**Co nanoparticles decorated with in-situ exsolved oxygen-storage $CeO_2$ for an efficient and stable electrolysis of pure $CO_2$**

**Lanying Lu [a], Debo He [b], Rong Fang [b], Chengsheng Ni [b] \* and John T.S. Irvine [b c]**


*a Chongqing Technology and Business University, Nan'an district, Chongqing, 400067 China*

*b College of Resources & Environment, Southwest University, Chongqing 400715, China*

*c College of Chemistry, University of St Andrews, North Haugh, Scotland KY16 9ST, UK*

**\* Corresponding author: nichengsheg@swu.edu.cn;**

**Abstract**

The valorization of the $CO_2$ greenhouse gas is important in decarbonization using the renewable energies. Intermediate temperature solid oxide electrolysis cells (SOEC) working at around 800 $^{\circ}$C can be useful in activating the strong C=O bond (799 kJ mol$^{-1}$) in $CO_2$ for the production of CO and decreasing the precious electricity by partially using the heat instead. Ceria/Co doping on the stable chromite is employed to design a composite oxide/metal cathode with a unique ceria decorating $Co^0$ for the direct $CO_2$ electrolysis. The *in situ* outgrowth of $Co^0$ from the B site activates the ceria exsolution from the A site, or *vice versa*, producing a well-adhered heterojunction for the activation of $CO_2$. A high current and stable density above 1 Acm$^{-2}$ for 300 hours is obtained at a bias of 1.3 V for the $CO_2$ at a Faraday efficiency close to unity. The higher electrochemical performance of the cell with Ce/$Co^0$ codoped cathode is explained by the oxygen storage property of the ceria rather than the direct activation of $CO_2$ over ceria. This work presents a novel method of constructing metal/oxide cathode for efficient $CO_2$ analysis and in-depth mechanistic explanation for the metal/oxide hetero-structure in $CO_2$ activation.

**1. Introduction**

The $CO_2$ emissions induced by the increasing consumption of fossil fuels has a significant impact on the global warming [1, 2]. The capture and efficient utilization of the produced $CO_2$ is one of the important ways of achieving a carbon-neutral production. Because of the high energy of the C=O bond (799 kJ mol$^{-1}$) [3], the reduction and valorization of $CO_2$ could be much favorable if it activated by thermal and electrical energy simultaneously for the production of CO and $O_2$.[4]

Solid oxide electrolysis cell (SOEC) operating at around 800 $^{\circ}$C can convert electric power into chemical energy for the dissociation of $CO_2$ at a high efficiency [5-8]. Comparing with the conventional Ni(O)-based cathode with the redox instability and tendency to induce carbon deposition, perovskite oxide electrode could be an attractive alternative providing their electrochemical catalysis was improved by the addition of a small amount of metal co-catalyst [9-12].

The infiltration or doping of reducible transition metals (Cu, Co, Ni et al.) on the B-sites of a stable perovskite has been investigated to improve the electrochemical performance for $CO_2$ electrolysis [13-17]. The doping of excessive reducible cations could decrease the stability of the perovskite, but under a well-designed doping level, the valence change of these reducible cations can increase the oxygen vacancies ($V_O$) for the transport of oxide-ion for expanded reaction area[5, 18, 19]. Specifically, if the exsolution of reducible cation is above the stable limit of the perovskite, well-dispersed metal particles on the parent perovskite can be used to enhance the catalytic activity [20-23].

The exsolution of B-site reducible cation from a stoichiometric $ABO_3$-type perovskite would induce the production of $AO_x$ or Ruddlesden-Popper (R-P) phase [6, 24-26]. The production of $AO_x$ could be $CeO_2$ if Ce was included on the A site. Because ceria showed a good oxygen storage ability (along with the production of $V_O$ in reduced atmosphere) [27] and a catalytic activity in the electrochemical $CO_2$ electrolysis [28], the simultaneous

production of ceria and metal particles on the surface could enhance the $CO_2$ electrolysis and inhibit the production of R-P phase. $Ce^{3+}$ (1.34 Å) could form a perovskite with Fe to produce a perovsikite (e.g. $CeFeO_3$) under an intermediate oxygen partial pressure ($P(O_2)$) [29], but the more stable $Ce^{4+}$ in air with an ionic radius (1.14 Å) in oxidizing atmosphere could induce strain on the perovskite lattice to impart a low solubility of $CeO_2$ in the perovskite[30, 31].

In this study, Ce and Co were doped simultaneously on the A and B site of $La_{0.7}Ca_{0.3}CrO_3$, respectively, for the simultaneous production of Ceria and $Co^0$ catalyst on the surface of perovskite-type chromite for the electrolysis of $CO_2$ at 800 ºC. A single-phase perovskite-type $La_{0.65}Ca_{0.3}Ce_{0.05}Cr_{0.9}Co_{0.1}O_3$ (Ce-LCCo) was prepared at 1350 ºC in air and the exsolution of $CeO_2$ and trace CoO was found during the re-oxidation at 1100 ºC for the calcination on the electrolyte. The SOEC with Ce-LCCo showed a very stable performance (1.05 A $cm^{-2}$ at around 1.3 V) for during the 300-h electrolysis using pure $CO_2$ without a prior reduction to generate metal particles. No trace of carbon deposition was found after the durability test, demonstrating that the combination of chromite, $CeO_2$ and Co nanoparticles was a promising cathode for $CO_2$ at 800 ºC. In contrast to previous research where ceria was stipulated to increase the reaction site by the ionic conductivity [32], the theoretical study indicates that the activation of the $CO_2$ was initiated by grabbing an oxygen atom from ceria to produce a carbonate bonding to the metal. The metal/oxide junction actually retards the CO desorption, but it facilitates the $CO_2$ electrolysis at large. This work is important in designing a metal/oxide composite cathode with special architecture of ceria decorating Co metal and highlighted the role of oxygen storage of oxides on for the direct $CO_2$ electrolysis.

## 2. Experimental section

### 2.1 Materials synthesis

$La_{0.7}Ca_{0.3}Cr_{1-x}Co_xO_3$ (x=0 and 0.1) are noted as LC, LCCo. $La_{0.65}Ca_{0.3}Ce_{0.05}Cr_{0.9}Co_{0.1}O_3$ is noted as the Ce-LCCo, All of Above mentioned perovskites were synthesized by the combustion method. Stoichiometric amounts of $Ce(NO_3)_2 \cdot 9H_2O$ (99.9% Macklin, China), $Co(NO_3)_2 \cdot H_2O$ (Macklin, 99%), $La(NO_3)_3 \cdot 9H_2O$ (Macklin, 99%) and $Cr(NO_3)_3 \cdot 9H_2O$ (Macklin, 99%), $CaCO_3$ (99.9% Macklin, China), were dissolved in deionized water to form the perovskite ingredients. Citric acid (1:1 in a molar ratio to the metal cations) as a complexing agent was added into the solution. After the precursor solution was heated and stirred to form a gel and then calcined at 600 ºC for 5 hours, the desired perovskites were obtained through calcination at 1300 ºC for 5 hours in air.

The powders of LSGM electrolyte were prepared through a solid-state reaction. Stoichiometric amounts of $SrCO_3$ (99.9% Macklin, China), $La_2O_3$ (99.9% Macklin, China), $Ga_2O_3$ (99.9% Macklin, China) and $MgO$ (99.9% Macklin, China) were ball-milled for 1.5 hours in ethanol, and then the desired admixture finished calcination at 800 °C for 5 hours in air. The powders after grinding again for 1 hour were pressed into a film, then LSGM electrolyte film were calcined subsequently at 1480 ºC for 5 hours to finish the desired dense level.

$La_{0.8}Sr_{0.2}CoO_3$ (LSC) was synthesized *via* the combustion method: Stoichiometric amounts of $La(NO_3)_3 \cdot 9H_2O$ (Macklin, 99%), $SrCO_3$ (Aladdin, 99.5%) and $Co(NO_3)_2 \cdot 6H_2O$ (Macklin, 99%) were dissolved in the deionized water containing citrate acid (1:1 in a molar ratio to the metal cations) as complexing agent. The solution was heated and stirred using a hotplate to form a viscous gel that was then calcined at 950 ºC for 5 hours to yield the cathode material.

2.2 Characterization techniques

X-ray diffraction (XRD) patterns of the prepared samples were acquired using a diffractometer ($K_{\alpha 1}$ =1.5406 Å, 36KV and 20 mA) in the $2\theta$ range from 10 ° to 80 ° at a step size of 0.01 °. The unit-cell parameters were calculated using the software Jade suite (Version 6.5.26, Materials Data Inc.). Bars of the electrode materials were cut into a rectangular bar of 4 x 3 x 13 mm$^3$ for the conductivity measurement, and four Ag wires were attached as probes. The conductivity was measured using a high-accuracy multimeter (Keithley 2100, United States) and a standard direct current (DC) four-probe method in air and 5% $H_2$. In order to explore the relationship between the conductivity and the oxygen partial pressure ($P(O_2)$)) using a zirconia sensor, pure Ar was used to purge the gas for 30 min at 800 °C before the injection of 5% $H_2$ for 5 hours. Temperature programmed reduction (TPR) was performed using a VDSorb-91i instrument (Vodo, China) equipped with a thermal conductivity detector (TCD), the flow of the analysis is 5% $H_2$ (20 ml min$^{-1}$). $CO_2$ desorption was performed on the reduced sample (800 °C in 5% $H_2$) after the aging in 10% $CO_2$ at 500 °C, and the $CO_2$ in the effluent of Ar carrier gas was monitored using a residual gas analyzer (RGA, QIC-20, Hiden, UK) during the heating. The temperature is in the range from 150 to 800 °C at 10 °C min$^{-1}$. The thermal expansion coefficients (TECs) were measured on a dilatometer (PCY-II, Xiangyi, China) at 5 °C min$^{-1}$ heating in air and cooling in 5% $H_2$, respectively. Thermogravimetric analyses (TGA) in 5% $H_2$ were recorded on a TG209 F3 tarsus instrument (NETZSCH, Germany). High-angle annular dark-field scanning transmission electron microscopy (HAADF-STEM, 200KV, TF20, FEI, USA) was performed on the electrode after durability of $CO_2$ electrolysis.

2.3 Cell fabrication and testing

For the single cell manufacturing, firstly, the powders of fuel electrode materials (LC, LCCo, Ce-LCCo) and air electrode materials (LSC) were mixed with an equal weight of vehicle containing polyvinyl butyral in terpineol to form a viscous slurry. Then the prepared slurry with fuel electrode materials were printed on the

one side of LSFM electrolyte of 0.3 mm in thickness and sintered at 1100 ℃ for 2 hours. For the other side of electrolyte, the slurry with air electrode material was printed and calcined subsequently at 1100 ℃ for 2 hours.

The electrochemical measurement of cell need preparation including that silver wires were pasted using the silver paste (Sinwe, Batch No. 3706, China) containing 20% starch for the current collection. The electrochemical performances of current-voltage (I-V), electrochemical impedance spectroscopy (EIS) and current-voltage (I-V) were measured on a Zennium Pro electrochemical workstation (Zahner, Germany). The sine wave of EIS measurement was in an amplitude of 10 mV from 1M Hz to 0.050 Hz, and the EIS data were fitted using the Zman software.

**Theoretical calculations**

A metal cluster containing 8 Co atoms was placed on the (100) surface of $Ce_8O_{16}$ supercell to construct the Co/ceria heterojunction. A vacant space of larger than 15 Å on the top of Co metal was used to simulate the vacuum state. The structure in 3D periodicity was relaxed in a Quantum-Espresso (QE) suite [33] using a cutting energy of 49 Ry. Electron−ion interactions were coupled with projected augmented wave pseudopotentials. Electron exchange and correlation effects were carried out generalized gradient approximation (Perdew−Burke−Ernzerhof). The Brillouin zone integration were used $3 \times 3 \times 3$ k point. A $CO_2$ molecule was put on the Co surface or Co-ceria interface to simulate the adsorption and the one CO molecule was removed from the adsorbed $CO_2$, leaving an oxygen on the surface to simulate the CO desorption. The distance between CO molecule and O atom was about 3 Å. A climbing image nudged elastic band (NEB) method was used to find the minimum energy paths of the desorption process. The $CO_2$ was decomposed into CO and O including initial, intermediate and last image, which define the diffusion coordinates along with the pathways [6].

## 3. Result and discussion

### 3.1 Material characterization

The pristine samples prepared at 1300 °C are monophasic perovskites according to the XRDs (**Figure 1**). Comparing to LC, the main peaks were found moving to high angle with Ce and Co elements doping on the A- and B- sites before and after the reheating, and to low angle after reduction process. There is no obvious phase variation in LCCo after the reheating at 1100 °C except for the production of traces of ceria. The reduction in 5% $H_2$ caused the production hexagonal close-packed (*hcp*) $Co^0$, while LCCo was maintained the perovskite structure without any sign of $Co^0$ on the surface. The presence of ceria after the reheating process could be ascribed to the oxidation process of $Ce^{3+}$ to $Ce^{4+}$. The exsolution of ceria indicates that the remnant perovskite could generate A-site deficiency that accelerated the Co exsolution from the lattice, since no Co metal was found in the reduced LCCo.
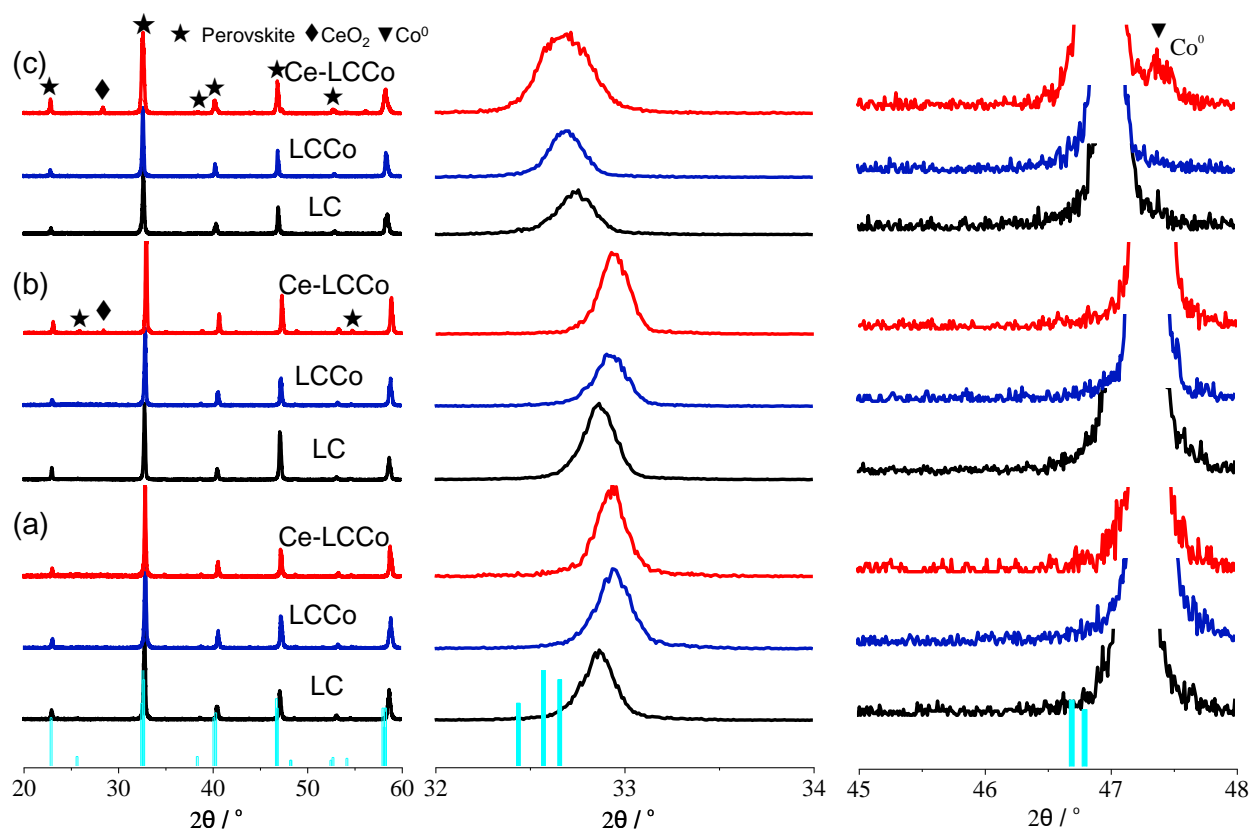
Figure 1. XRDs of as-prepared LC, LCCo, Ce-LCCo (a), reheated at 1100 °C in air (b), and reduced at 800 °C 5% $H_2$ for 5 hours (c). The Powder Diffraction File (PDF: 33-701) for $LaCrO_3$ were plotted at the bottom for comparison. The regional magnification of the XRD was provided to show the shift of the main peak and the presence of $Co^0$.

The $CoO_x$ doping expanded the lattice expansion of the chromite perovskite while the Ce/Co codoping caused the lattice shrinkage (**Table 1**). The lattice expansion could be ascribed to the incorporation of larger $Co^{3+/2+}$ (0.61 Å / 0.745 Å) on the site of $Cr^{4+/3+}$ (0.55 Å / 0.615 Å) while the further doping of $Ce^{4+}$ (0.87Å) with smaller ionic radius than $La^{3+}$ (1.032 Å)) caused the contraction of the unit cell. The $Co^{2+}$ (0.745 Å) [34] partial substituting $Cr^{3+}$ (0.615 Å) does not offset the impact of lattice shrinking occurred to the substitution of $Ce^{4+}$ (1.14 Å) for $La^{3+}$ (1.36 Å) site. Actually the $Ce^{4+}$ donor on $La^{3+}$ site could also cause the reduction of B site cation as a result of the electron neutrality, but the lattice shrinkage of Ce-LCCo from LCCo indicates $Ce^{4+}$ reside actually on the A site of the perovskite. The reheating in air caused the absorption of oxygen, causing the shrinkage of the unit cell along with the production of the higher-valence cation on the B site and LC, LCCo and Ce-LCCo. The cell contraction in the oxidation is also consistent with the cell expansion during the reduction in 5% $H_2$ at 800 °C for 5 hours.

Table 1. Unite cell parameters of the pristine samples compared to those treated under oxidation in air and reduction in 5% $H_2$. The error of calculation is included in the parenthesis at the end of each number.

| Samples [a] | a / Å | b / Å | c / Å | V / Å³ |
| --- | --- | --- | --- | --- |

| | | | | |
|---|---|---|---|---|
| LC | 5.437(4) | 5.422(5) | 7.681(9) | 226.49 |
| LCCo | 5.450(7) | 5.388(6) | 7.714(5) | 226.58 |
| Ce-LCCo | 5.441(0) | 5.406(0) | 7.689(2) | 226.17 |
| LC-RH | 5.414(7) | 5.422(1) | 7.697(0) | 225.97 |
| LCCo-RH | 5.434(8) | 5.422(0) | 7.682(7) | 226.39 |
| Ce-LCCo-RH | 5.441(0) | 5.406(0) | 7.679(2) | 225.87 |
| LC-Red | 5.458(1) | 5.461(2) | 7.730(2) | 230.42 |
| LCCo-Red | 5.483(9) | 5.486(2) | 7.724(0) | 232.38 |
| Ce-LCCo-Red | 7.594(1) | 4.659(3) | 6.505(1) | 230.17 |

*a*: suffix of "-RH" and "-Red" denotes reheating at 1100 ℃ in air and reduction at 800 ℃ in 5% $H_2$ for 5 hours, respectively.

The weight loss TGA (**Figure 2(a)**) for LC, LCCo and Ce-LCCo in 5% $H_2$ indicates that Co doping increase the oxygen loss from the perovskite lattice and the reheated Ce-LCCo shows the largest weight loss (1.85%) than the as-prepared sample. The differential thermogravimetry (DTG, **Figure 2(b)**) of LC showed two peaks at 503 and 706 ℃ because of the oxygen loss from the perovskite lattice accompanied by the reduction of $Cr^{4+}$ to $Cr^{3+}$. The Co doping on the B site decreased the DTG peaking temperature to 397 ℃, while the additional $Ce^{4+}$ doping in LCCo increased the temperature to 482 ℃. The temperature variation because of the oxide-ion conductivity of the perovskite was enhanced by $Co^{2+/3+}$ acceptor doping but was decreased by the $Ce^{4+}$ donor doping. The reheating of Ce-LCCo in air at 1100 ℃ will increase the initial oxygen content of the perovskite, causing more weight loss in 5% $H_2$ and the superficial $CeO_2$ exsolution would promote the oxygen loss at lower temperature because $CeO_2$ can act as an oxygen transfer channel [35]. The peak temperature shifting in DTG is generally consistent with that in TPR peak (**Figure 2(c)**), but the more pronounced decrease of reduction temperature of the reheated Ce-LCCo would be

related to the superficial oxygen loss. The higher ramp rate of TPR than TGA, and is an evidence for the accelerated oxygen loss on the surface by $CeO_2$ exsolution.
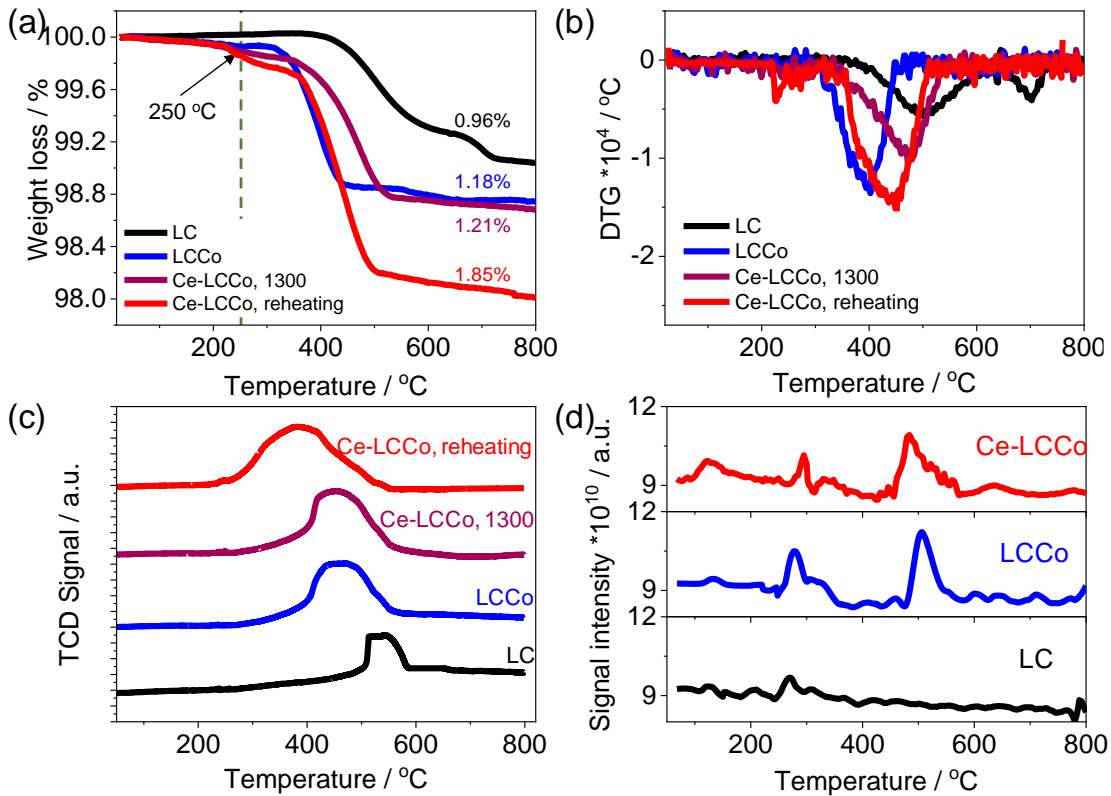


Figure 2 (a) TGA and (b) DTG of the perovskite under flowing 5% $H_2$; (c) TPR of the oxides in 5% $H_2$ and (d) $CO_2$ desorption of the perovskites after a previous annealing in $CO_2$.

The bonding between the electrode and the electrolyte during the thermal cycling depends on the matching in TECs of the components, so dilatometry was measured in air and 5% $H_2$ (**Figure 3(a) & Table S1**). Co doping in LC increased the TEC in air from 18.05 to 13.98 ppm $K^{-1}$, while Ce-LCCo showed a similar TEC (15.95 ppm $K^{-1}$) to that of LC. The increased TEC in LCCo in air could be related to the chemical expansion induced by the spin transition of $Co^{3+}$ during the heating process, because the chemical expansion induced by the reduction of cations could have resulted in an expansion transition at 250 to 300 $^{\circ}$C.
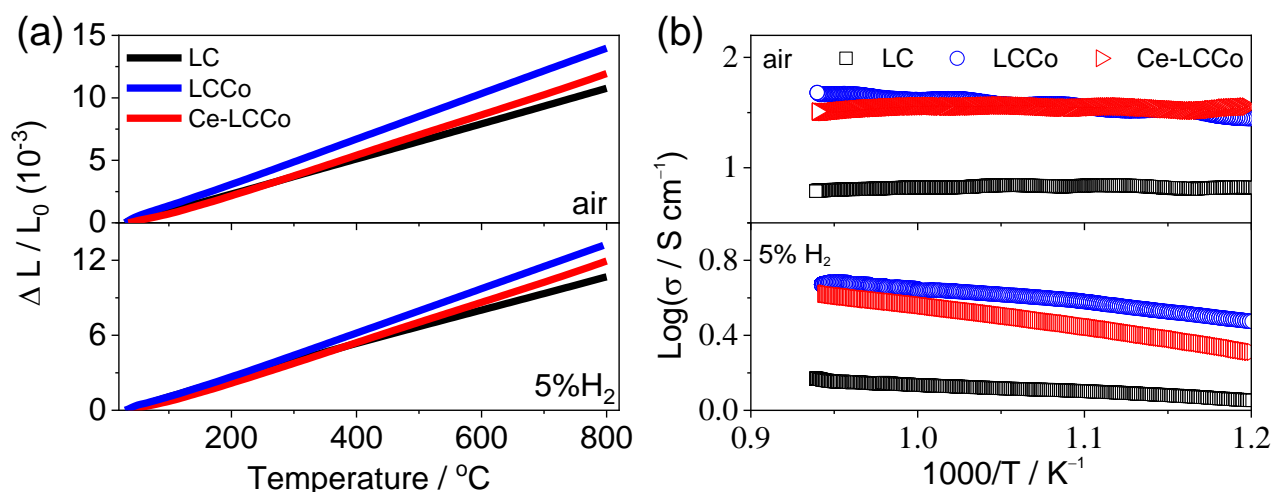
Figure 3 (a) Dilatometry and (b) Arrhenius plots of the electrical conductivity of LC, LCCo and Ce-LCCo in air and 5% $H_2$. The sample in 5% $H_2$ was pre-reduced at 800 $^{\circ}$C for 5 hours.

The Co doping in LC increased the conductivity of LC by one order of magnitude in air. One may argue that the transition of $Co^{3+}$-O-$Co^{2+}$ could be the reason for the transport of charge carriers (electron or electron holes), but the small amount (10 at.% on B site) of Co cation was insufficient to percolate the perovskite to produce such effect. The increased conductivity could be related to the acceptor doping of $Co^{3+/2+}$ on $Cr^{3+/4+}$ to increase the amount of $Cr^{4+}$ for more charge carriers through $Cr^{4+}$-O-$Cr^{3+}$. The acceptor doping effect could also explain the higher electric conductivity of LCCo and Ce-LCCo than LC in 5% $H_2$. Although the electric conductivity decreased in the reducing atmosphere, it is still high enough (> 0.1 $Scm^{-1}$) to be used for the cathode of an SOEC.

3.2 Electrochemical performance of cells

For chromite as a *p*-type oxide boasting high conductivity in air, the pre-reduction before the electrolysis of $CO_2$ is actually mandatory. The cathodic current or produced CO is able to reduce the cathode for the exsolution of $Co^0$ or ceria from the oxide lattice. The IV curve (**Figure 4(a)**) of the electrolysis cell after 24-h durability at around 1.3 V showed that an abrupt increase in current density was observed when the bias is

higher than 0.92 V because of the depolarization by $CO_2$ on the cathode. Specifically, the current density of the cell with Ce-LCCo cathode (-1.27 A cm$^{-2}$ @ −1.4 V) was much higher than the one with either LCCo or LC cathode (-0.93 @ −1.4 V). The dynamic EIS at -1.2, -1.4 and -1.6 V (**Figure 4(b)**) were in accord with the IV curve in the electrolysis range since the polarization resistance ($R_p$) of cell with Co-LCCo cathode was the smaller amongst the three cells. According to the DRT calculations (**Figure S1**), Co doping in LC accelerated the low frequency peak (P1) for the adsorption and activation of $CO_2$, while peaks (P2 and P3) at the intermediate frequency was suppressed significantly by the $CeO_2$ exsolution in Ce-LCCo. As P2 and P3 was ascribed to the surface electron transfer for the production of CO, $CeO_2$ was found to accelerate the reduction of adsorbed $CO_2$.[36]
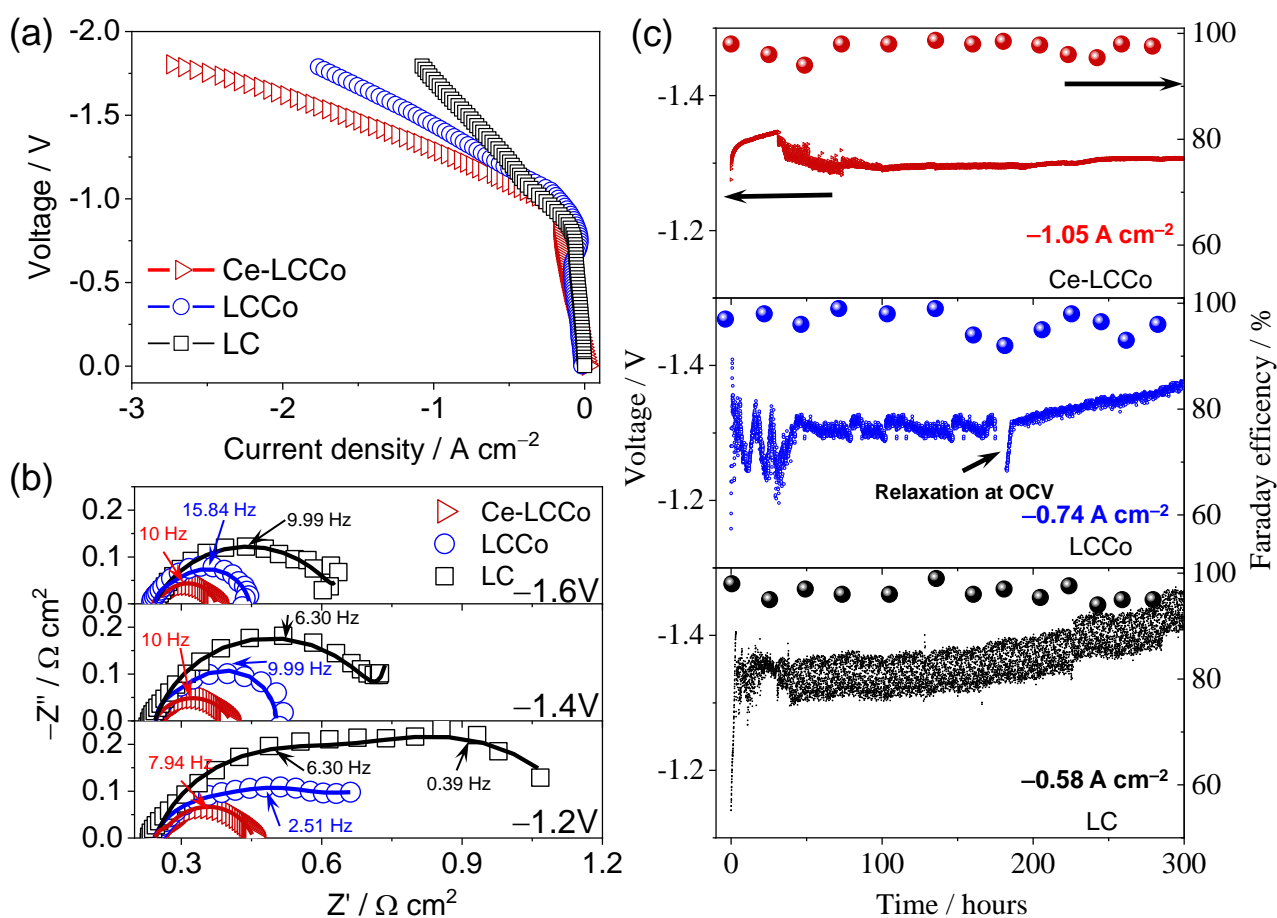
Figure 4. IV (a) and dynamic EIS of the electrolysis cells at 800 °C for the electrolysis of pure $CO_2$. (c) Chronoamperometry and Faraday efficiency for LC, LCCo and Ce-LCCo cell at -0.58, -0.74 and -1.05 $Acm^{-2}$. The current density are selected to impart an initial bias around -1.3 V for each cell.

The chronoamperometry of the cells under an initial bias around -1.3 V (**Figure 4(c)**) showed a sluggish voltage within the first 50 hours. The Ce-LCCo cell showed a gradual increase in voltage to -1.33 V and then a stable level at -1.29 V for a current density of -1.05 A $cm^{-2}$, which the LCCo cell showed an oscillating voltage variation at -0.74 A $cm^{-2}$ until it stabilized at -1.32 V at 48.5 hour. The LC cell showed a gradual voltage increase after the first 144-hour stability, reaching -1.43 V within the 300-hour chronoampermetry. On the contrary, the voltage variation of the Ce-LCCo cell after 50 h was minor, stabilizing in the range from -1.30 to -1.31 V. The initial fluctuation of the voltage could be explained by the structure change in the cathode: the oxygenated Ce-LCCo would produce $Co^0$ and ceria upon the application of cathodic current. The production of $Co^0$ in Ce-LCCo would be easier than that in LCCo where the initiation of $Co^0$ exsolution from the oxide lattice involving the nucleation and thermal growth.

The low-resolution microstructure of the LC cell (**Figure S2**) maintained the porous structure and adhered very well to the electrolyte. The grain size of the chromite perovskite was around 100 nm (**Figure 5**) while the particle size is on the scale of micrometers. The microstructure of the Ce-LCCo cell at 30- and 300-h stability was quite similar to the one of LC after 300-h stability at a low-magnification (**Figure S2**), indicating the chromite backbone was stable for the cell working at 800 °C. However, the oxide matrix of the Ce-LCCo cathode at 30-h stability showed a larger grain size (around 500 nm) than the one at 300-h stability (100 nm), indicating the durability test under cathodic current would impose the partial pulverization of the cathode.
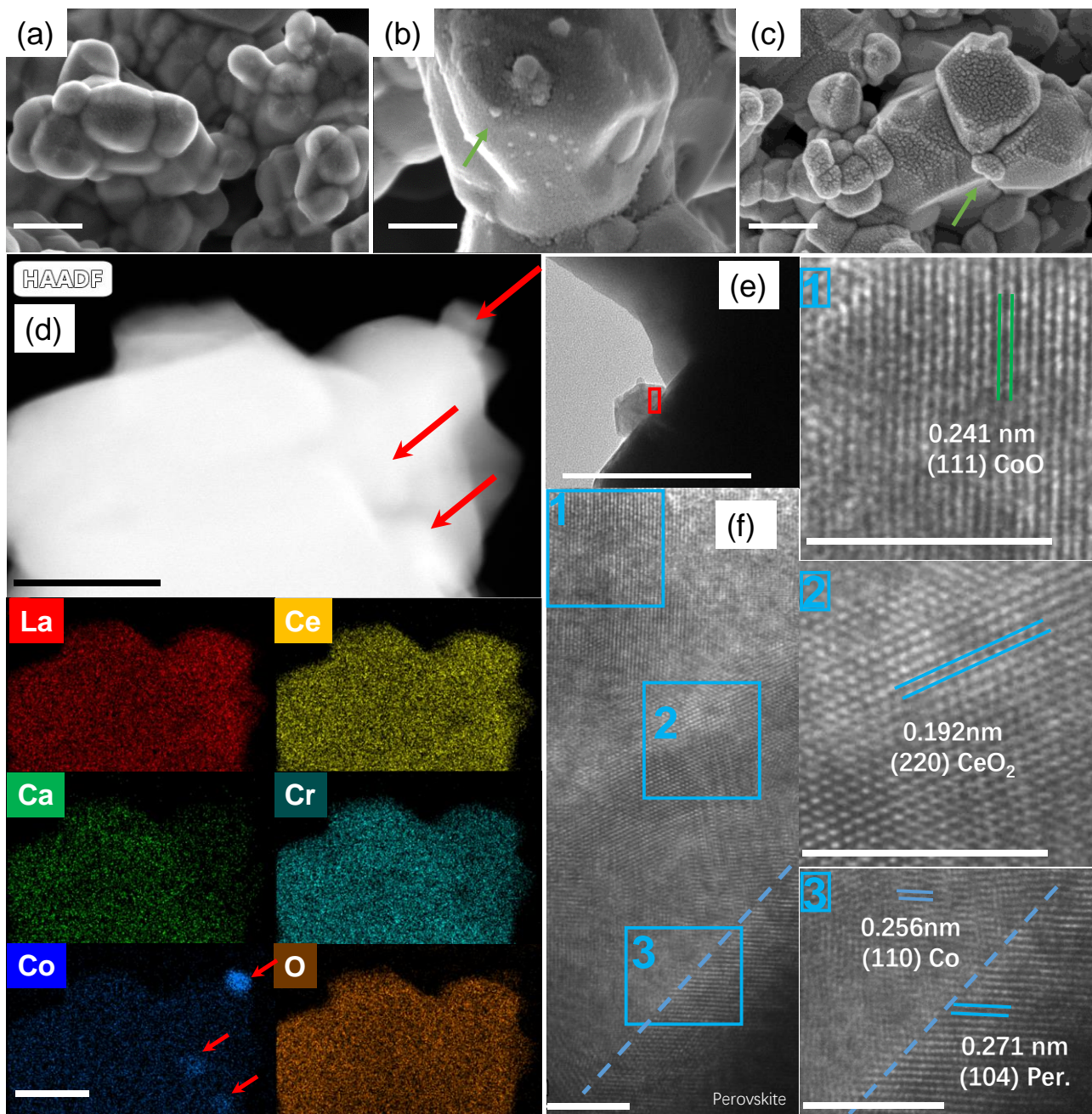
Figure 5. SEM images of the LC (a) after 300 hours' durability and the Ce-LCCo cathode after 30 (b) and 300 hours' durability (c). HAADF and EDS (d-f) of the Ce-LCCo cathode after 300 hours' durability for $CO_2$ electrolysis. The arrows in (d) indicates the area of outgrown particles after the durability test. ①-③ representative the magnified images in (f) at the corresponding locations. The arrows in (b-c) indicates the exsolved particles. The scale bars in image (a-e) represent 200 nm while the rest indicate 2.5 nm. "Per." denotes the perovskite matrix.

Distinct particles (30 nm in size) outgrown from the Ce-LCCo cathode after the 30 hours'

chronoamperometry, but these particles gradually grow to the size of around 100 nm in diameter. More

importantly, the density of these particles increased with the durability test. HAADF image with EDS mapping

(**Figure 5(d)**) confirmed the presence of Co enriched particles that (**Figure 5(e) & (f)**) exhibited CoO on the

outer surface were coated by ceria since the EDS of these particles showed a weak Ce element on the outer

fringe. Fine particles for ceria was also found on the interface of the exsolved particles and the perovskite matrix,

which is consistent with the SEM image where fine ceria nodules was found the surface of Co nanoparticles.

The Co particles was much smaller at 30 hours' durability than those after 300 hours' durability, but the high

bias indicates the size of Co was not the predominant factor the electrolysis of $CO_2$.

### 3.3. Theoretical calculations

As a high-energy surface, the direct relaxation of $CO_2$ on the surface of (100) surface of ceria could cause

the destruction of the surface, but the addition of $Co^0$ on the surface would induce a stable metal/oxide

heterojunction (**Figure S3**). The Ce-O bond length in the heterstructure (2.64 Å) is longer than that in a ceria

oxide (2.30 Å), while the Co-O bond (1.93 Å) is shorter than that in a normal CoO (2.12 Å). The adsorption

energy of $CO_2$ (2.50 eV, **Figure 6(a) & (b)**) is much higher than the on $Co^0$ (0.68 eV), indicating the Co/ceria

interface could be the idea place for $CO_2$ activation. Interestingly, the presence of vacancies on the $Co^0$/ceria

interface actually is not conducive for the activation of $CO_2$. $CO_2$ on the interface forms a bi-dentate $CO_3^{2-}$ on

the metal side (**Figure 6(c) & (e)**) while $CO_2$ on $Co^0$ particles (**Figure 6(d) & (f)**) generate Co-C and Co-O

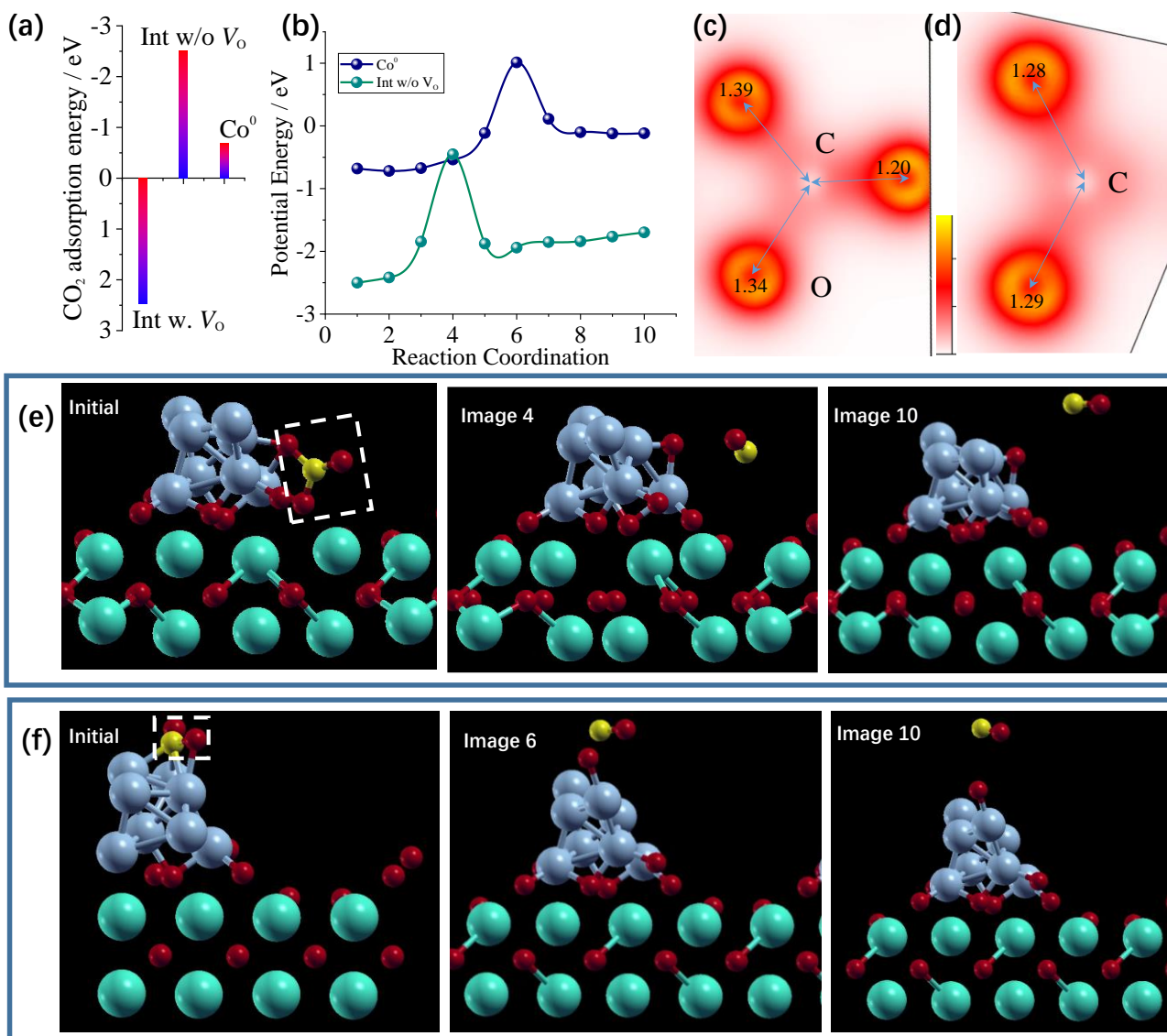bonds twisting the straight $CO_2$ into a tilted angle.

Figure 6. (a) $CO_2$ adsorption energy on Co/ceria interface with (Int w. $V_O$) and without (Int w/o $V_O$) oxygen vacancy or the one on Co metal ($Co^0$). (b) Potential energy of the adsorbed $CO_2$ on the way to produce CO. Charge density of the adsorbed $CO_3^{2-}$ on the interface (c) or $-CO_2$ on $Co^0$ (d) in the dashed rectangle of initial images in (e) and (f) showing de-adsorption process from the interface and the top of $Co^0$, respectively. C – O bond lengths (in Å) were indicated in (c) and (d). "Image 4" in (e) and "image 6" in (f) are selected for the highest potential energy. Ce (green), O (red), Co (gray) and C (yellow) are drawn in atomic size.

The configuration of $CO_2$ activation on the Co/ceria interface implies the donation of oxygen from ceria, which is consistent with the long Ce-O bond that could be readily donating an O anion from the interface. The oxide ion from the dissociated $CO_2$ will transport to the interface to fill in the vacancy and thus the Co on oxygen-deficient ceria is not considered in the reaction route of a cathode. The charge density on the two C=O bonds on the Co side in the adsorbed $CO_3^{2-}$ is lower than the one in $–CO_2$, which is consistent with their longer bond lengths.

The presence of oxide near Co greatly enhanced the adsorption of CO, [37] and this is in accord of the higher energy barrier (2.0 eV *versus* 1.7 eV) for the CO dissociation from the interface in the reaction route calculation than the one from the top of $Co^0$. However, considering the high $CO_2$ affinity, the CO produced from the $Co^0$/ceria interface is more favored than the latter.

## 4. Discussions

The desorption of $CO_2$ will not cause the re-oxidation of the reduced $CeO_2$ according to the $^{13}CO$ detection[38], but the superficial oxygen mobility was found to be critically important for the electrolysis of $CO_2$. Therefore, the calculation of the (100) surface of ceria with higher surface energy than either (110) or (111) surface could be more meaningful [39]. The (100) surface was chosen also because it was the possible transport plane of the oxide ions [40].

Theoretical calculations indicates the (111) surface of ceria can activate $CO_2$ to produce a monodentate layer similar to noble metals [41], such as Pt, Rh and Pd, but the addition of 0.01 mol% Pt on samaria-doped ceria cathode enhanced the $CO_2$ electrolysis by 56% [42], indicating a synergistic effect between the metal and oxide interface.

According to the DFT calculation, the metal provides the place for the anchoring of $CO_2$ or $CO_3^{2-}$ while the oxides provide the oxygen for the activation. The DFT calculation of the Co on (100) surface of ceria indicates that ceria was important in providing the oxygen for the activation of $CO_2$ in the form of $CO_3^{2-}$ on Co metal surface. The addition of oxygen storage oxides on Ni metal could provide fast oxygen transfer in the cathode,[43] but we further confirmed that they enhance the activation of $CO_2$ by oxygen donation to produce carbonate for an continuous operation under pure $CO_2$ feeding gas. In the case of pure $CO_2$ feeding, the accumulated oxygen left behind by the CO removal will decrease the $CO_2$ activation on metal surface, as can been that a significant degradation was found in the degradation of SOEC using $CO_2$ feedstock (**Table 2**) unless ceria was used on the cathode side. This could explain the degradation of the cell with LCCo cathode where $Co^0$ was also present on the surface since LC backbone is not able to re-adsorb the oxygen left on the metal surface.

Table 2. The durability-test comparison of perovskite cathodes for pure-$CO_2$-fuel SOEC.

| Cathode | Electrolyte | Current density /Acm$^{-2}$ @bias / V | Degradation (temp./ $^{o}$C) | Duration (h) | |
|---|---|---|---|---|---|
| **La$_{0.65}$Ca$_{0.3}$Ce$_{0.05}$Cr$_{0.9}$Co$_{0.1}$O$_3$** | **LSGM** | **1.05 @1.3** | **1% (800)** | **300** | |
| LaSrFeO$_{4+\delta}$ | LSGM | 0.96 @1.2 | 53% (850) | 100 | [44] |
| La$_{0.3}$Sr$_{0.7}$Fe$_{0.7}$Ti$_{0.3}$O$_{3-\delta}$ | LSGM | 0.27 @1.5 | 11% (800) | 24 | [45] |
| La$_{0.6}$Sr$_{0.4}$Fe$_{0.95}$Mo$_{0.05}$O$_{3-\delta}$-GDC | SSZ | 0.86 @1.2 | 23% (800) | 30 | [46] |
| La$_{0.6}$Sr$_{0.4}$Fe$_{0.8}$Ni$_{0.2}$O$_{3-\delta}$ | YSZ | 0.40 @1.5 | 25% (800) | 35 | [47] |
| La$_{0.4}$Sr$_{0.6}$Co$_{0.2}$Fe$_{0.7}$Mo$_{0.1}$O$_{3-\delta}$-GDC | LSGM | 0.65 @1.2 | 23% (800) | 100 | [48] |
| Ni-SrFeO$_{3-\delta}$ | LSGM | 0.50 @1.4 | 10% (800) | 100 | [49] |

| | | | | | |
|---|---|---|---|---|---|
| $(Sr_{0.95})_{0.9}(Ti_{0.8}Nb_{0.1}Mn_{0.1})_{0.9}Fe_{0.1}O_{3-\delta}$-SDC | YSZ | 0.20 @1.6 | 15% (800) | 24 | [50] |
| $Sr_2Fe_{1.35}Mo_{0.45}Co_{0.2}O_{6-\delta}$-GDC | LSGM | 0.40 @1.2 | 25% (800) | 220 | [51] |
| $Sr_2Fe_{1.5}Mo_{0.5}O_{6-\delta}$-SDC | LSGM | 1.12 @1.5 | 7% (800) | 100 | [52] |
| $La_{0.7}Sr_{0.3}Cr_{0.5}Mn_{0.5}(NiCu)_{0.075}$ | LSGM | 0.36 @1.2 | 16% (800) | 100 | [53] |
| $La_{0.5}Sr_{0.5}Fe_{0.95}V_{0.05}$-GDC | YSZ | 0.29 @1.2 | 17% (800) | 21 | [54] |
| $SrFeO_{3-\delta}$-SDC-Ni | LSGM | 0.50 @1.4 | 8% (800) | 100 | [49] |
| $(La_{0.2}Sr_{0.8})_{0.95}Ti_{0.55}Mn_{0.35}Cu_{0.1}O_{3-\delta}$ | LDC/ LSGM | 1.0 @1.4 | None (800) | 100 | [55] |
| $Sr_2Fe_{1.5}Mo_{0.5}O_{3-\delta}$-SDC | LSGM | 1.09 @1.5 | 2.7% (800) | 100 | [56] |

The electrolysis of $CO_2$ was dependent not only on the activation of $CO_2$, but also the desorption of CO from the surface, leaving an oxide ion on the surface of the oxides to be transported to the electrode/electrolyte interface. Surprisingly, the metal/oxide surface actually does not facilitate the desorption of CO. Because the CO adsorption energy on metal particles was found to decrease with the growth of metal particles[57], the growth of Co along the durability test could enhance the production of CO since ceria particles were also found to be covering the Co surface at the end of the durability test. The growth of metal particles will decrease the length of the metal/oxide interface but facilitate the desorption of CO [58]. The microstructure variation could affects the reaction sites and the adsorption energy of the reactive species to induce the fluctuating voltage for the cell with LCCo or Ce-LCCo cathode in the initial 50 hours' durability for $CO_2$ electrolysis.

The growth of metal particles from the oxide matrix will follow the second Fick's low and level off after the initial change [59]. The kinetics of particle growth could last the whole 300 hours, but it was more obvious at the initial stage and is affected by the diffusion of the cobalt cation to the surface and depletion of Co in the perovskites. After the exsolution is completed, the growth of particles (in size and amount) would level off.

The simultaneous infiltration of metal and ceria was used to enhance the electrocatalysis of an solid oxide cell [60], but the simultaneous exsolution created a unique structure where ceria can reside on the surface of an metal particles that is subjected to thermal growth. The special structure was enabled by the fact that the more metal outgrowth from the B site induced more ceria exsolution from the A site, or *vice versa*.[18, 19] The disconnected ceria was not supposed to enhance the ionic conductivity, but it could induce the activation of $CO_2$ on the ceria/$Co^0$ interface via the $CO_3^{2-}$ production since the equipotential of the metal and oxygen storage of ceria. The spillover of oxygen on the cobalt metal is in this respect very important for the transport of oxygen to the electrode/electrolyte interface [61].

**Conclusions**

A highly stable oxide cathode was constructed using in situ growth of metal/oxide composite by doping Co and ceria on the B and A site of chromite. Comparing to the LC cathode, the unique ceria dispersion on Co particles was achieved by the simultaneous ceria and $Co^0$ exsolution from A and B site. The Ce-LCCo cathode further improved the electrolysis of the cell than LCCo and the stability after 300 hours for the direct electrolysis of pure $CO_2$ feedstock. Ce doping in LCCo increased the performance of the electrode after an initial fluctuation in performance before it reached a stable electrolysis of $CO_2$. The metal/oxide interface was found to be critically important for the activation of $CO_2$ and the oxygen storage of the oxides is important for the removal of oxygen to regenerate the oxygen surface. Unlike the previous route where $V_O$ over an oxide anode was critically

important for the activation of $CO_2$, the oxygen storage of the adjacent oxide dominates the activation of $CO_2$ over metals in the metal/oxide heterojunction.

**References**

1.    Zhang, H. M.;    Li, L. S.;    Cao, J.;    Zhao, M. N.; Wu, Q., Comparison of renewable energy policy evolution among the BRICs. *Renew. Sust. Energ. Rev.* **2011,** *15* (9), 4904-4909.

2.    Matthews, H. D.; Wynes, S., Current global efforts are insufficient to limit warming to 1.5 °C. **2022,** *376* (6600), 1404-1409.

3.    Pandiyan, A.;    Kyriakou, V.;    Neagu, D.;    Welzel, S.;    Goede, A.;    van de Sanden, M. C. M.; Tsampas, M. N., CO2 conversion via coupled plasma-electrolysis process. *J. CO2 Util.* **2022,** *57*, 101904.

4.    Hauch, A.;    Kungas, R.;    Blennow, P.;    Hansen, A. B.;    Hansen, J. B.;    Mathiesen, B. V.; Mogensen, M. B., Recent advances in solid oxide cell technology for electrolysis. *Science* **2020,** *370* (6513), eaba6118.

5.    Ni, C. S.;    Zhou, J.;    Zhang, Z. Y.;    Li, S. B.;    Ni, J. P.;    Wu, K.; Irvine, J. T. S., Iron-based electrode materials for solid oxide fuel cells and electrolysers. *Energy Environ. Sci.* **2021,** *14* (14), 6287-6319

6.    He, D. B.;    Ruan, W. J.;    Li, J. B.;    Ni, J. P.; Ni, C. S., Heterogeneity in the Mo doped $La_{0.55}Sr_{0.45}FeO_3$ cathode for direct CO2 electrolysis. *Chem. Eng. J. (Lausanne)* **2022,** *433*, 133632.

7.    Liu, Q.;    Li, R.;    Feng, W.;    Li, J.;    Zhang, X.;    Lv, H.;    Shen, Y.;    Song, Y.;    Wang, G.; Bao, X., Promoting High-Temperature Oxygen Evolution Reaction via Infiltration of $PrCoO_{3-d}$ Nanoparticles. *ACS Appl. Energ. Mater.*

8.    He, F.;    Hou, M.;    Zhu, F.;    Liu, D.;    Zhang, H.;    Yu, F.;    Zhou, Y.;    Ding, Y.;    Liu, M.; Chen, Y., Building Efficient and Durable Hetero-Interfaces on a Perovskite-Based Electrode for Electrochemical $CO_2$ Reduction. *Adv. Energy Mater.* **2022,** *12* (43), 2202175.

9.    Liu, S. B.;    Liu, Q. X.; Luo, J. L., CO2-to-CO conversion on layered perovskite with in situ exsolved Co-Fe alloy nanoparticles: an active and stable cathode for solid oxide electrolysis cells. *J. Mater. Chem. A* **2016,** *4* (44), 17521-17528.

10. Liu, S.;    Liu, Q.; Luo, J.-L., Highly Stable and Efficient Catalyst with In Situ Exsolved Fe-Ni Alloy

Nanospheres Socketed on an Oxygen Deficient Perovskite for Direct CO2 Electrolysis. *ACS Catal.* **2016,** *6* (9), 6219-6228.

11. Tezel, E.;   Whitten, A.;   Yarema, G.;   Denecke, R.;   McEwen, J.-S.; Nikolla, E., Electrochemical Reduction of $CO_2$ using Solid Oxide Electrolysis Cells: Insights into Catalysis by Nonstoichiometric Mixed Metal Oxides. *ACS Cata.* **2022,** *12* (18), 11456-11471.

12. Zhang, D.;   Wang, Y.;   Peng, Y.;   Luo, Y.;   Liu, T.;   He, W.;   Chen, F.; Ding, M., Novel high-entropy perovskite-type symmetrical electrode for efficient and durable carbon dioxide reduction reaction. *Advanced Powder Materials* **2023,** *2* (4), 100129.

13. Xu, S. S.;   Li, S. S.;   Yao, W. T.;   Dong, D. H.; Xie, K., Direct electrolysis of $CO_2$ using an oxygen-ion conducting solid oxide electrolyzer based on $La_{0.75}Sr_{0.25}Cr_{0.5}Mn_{0.5}O_3$-delta electrode. *J. Power Sources* **2013,** *230*, 115-121.

14. Song, Y. F.;   Zhang, X. M.;   Xie, K.;   Wang, G. X.; Bao, X. H., High-Temperature $CO_2$ Electrolysis in Solid Oxide Electrolysis Cells: Developments, Challenges, and Prospects. *Adv. Mater.* **2019,** *31* (50), e1902033.

15. Liu, S.;   Liu, Q.; Luo, J.-L., Highly Stable and Efficient Catalyst with In Situ Exsolved Fe–Ni Alloy Nanospheres Socketed on an Oxygen Deficient Perovskite for Direct CO2 Electrolysis. *ACS Cata.* **2016,** *6* (9), 6219-6228.

16. Ansari, H. M.;   Addo, P. K.;   Mulmi, S.;   Yuan, H.;   Botton, G. A.;   Thangadurai, V.; Birss, V. I., Deciphering the Interaction of Single-Phase $La_{0.3}Sr_{0.7}Fe_{0.7}Cr_{0.3}O_{3-\delta}$ with $CO_2/CO$ Environments for Application in Reversible Solid Oxide Cells. *ACS Appl. Mater. Inter.* **2022,** *14* (11), 13388-13399.

17. Zhang, B. W.;   Zhu, M. N.;   Gao, M. R.;   Xi, X. A.;   Duan, N. Q.;   Chen, Z.;   Feng, R. F.;   Zeng, H. B.; Luo, J. L., Boosting the stability of perovskites with exsolved nanoparticles by B-site supplement mechanism. *NATURE COMMUNICATIONS* **2022,** *13* (1).

18. Li, B. X.;   He, S.;   Li, J. B.;   Yue, X. L.;   Irvine, J. T. S.;   Xie, D. T.;   Ni, J. P.; Ni, C. S., A Ce/Ru Codoped $SrFeO_{3-\delta}$ Perovskite for a Coke-Resistant Anode of a Symmetrical Solid Oxide Fuel Cell. *ACS Catal.* **2020,** *10* (24), 14398-14409.

19. Li, B.;   Irvine, J. T. S.;   Ni, J.; Ni, C., High-performance and durable alcohol-fueled symmetrical solid oxide fuel cell based on ferrite perovskite electrode. *Appl. Energy* **2022,** *306*, 118117.

20. Rath, M. K.; Lee, K. T., Investigation of aliovalent transition metal doped $La_{0.7}Ca_{0.3}Cr_{0.8}X_{0.2}O_3$-delta (X= Ti, Mn, Fe, Co, and Ni) as electrode materials for symmetric solid oxide fuel cells. *Ceram. Int.* **2015,** *41* (9), 10878-10890.

21. Carrillo, A. J.;   Kim, K. J.;   Hood, Z. D.;   Bork, A. H.; Rupp, J. L. M., $La_{0.6}Sr_{0.4}Cr_{0.8}Co_{0.2}O_3$ Perovskite Decorated with Exsolved Co Nanoparticles for Stable $CO_2$ Splitting and Syngas Production. *ACS Appl. Energ. Mater.* **2020,** *3* (5), 4569-4579.

22. Hou, Y.;   Wang, L.;   Bian, L.;   Wang, Y.; Chou, K.-c., Excellent Electrochemical Performance of $La_{0.3}Sr_{0.7}Fe_{0.9}Ti_{0.1}O_{3-\delta}$ as a Symmetric Electrode for Solid Oxide Cells. *ACS Appl. Mater. Inter.* **2021,** *13* (19), 22381-22390.

23. Zhang, S.;   Jiang, Y.;   Han, H.;   Li, Y.; Xia, C., Perovskite Oxyfluoride Ceramic with In Situ Exsolved Ni–Fe Nanoparticles for Direct $CO_2$ Electrolysis in Solid Oxide Electrolysis Cells. *ACS Appl. Mater. Inter.* **2022,** *14* (25), 28854-28864.

24. Hu, S. Q.;   Zhang, L. X.;   Liu, H. Y.;   Li, W. P.;   Cao, Z. W.;   Cai, L. L.;   Zhu, Y.;   Zhu, X. F.; Yang, W. S., Detrimental phase evolution triggered by Ni in perovskite-type cathodes for $CO_2$ electroreduction. *J. Energy Chem.* **2019,** *36*, 87-94.

25. Li, Y.;   Li, Y.;   Zhang, S.;   Ren, C.;   Jing, Y.;   Cheng, F.;   Wu, Q.;   Lund, P.; Fan, L., Mutual Conversion of CO–$CO_2$ on a Perovskite Fuel Electrode with Endogenous Alloy Nanoparticles for Reversible

Solid Oxide Cells. *ACS Appl. Mater. Inter.* **2022,** *14* (7), 9138-9150.

26. Park, S.; Kim, Y.; Han, H.; Chung, Y. S.; Yoon, W.; Choi, J.; Kim, W. B., In situ exsolved Co nanoparticles on Ruddlesden-Popper material as highly active catalyst for CO2 electrolysis to CO. *Appl. Catal. B* **2019,** *248*, 147-156.

27. Skorodumova, N. V.; Simak, S. I.; Lundqvist, B. I.; Abrikosov, I. A.; Johansson, B., Quantum Origin of the Oxygen Storage Capability of Ceria. *Phys. Rev. Lett.* **2002,** *89* (16), 166601.

28. Green, R. D.; Liu, C. C.; Adler, S. B., Carbon dioxide reduction on gadolinia-doped ceria cathodes. *Solid State Ionics* **2008,** *179* (17-18), 647-660.

29. Robbins, M.; Wertheim, G. K.; Menth, A.; Sherwood, R. C., Preparation and Properties of Polycrystalline Cerium Orthoferrite (Cefeo3). *J. Phys. Chem. Solids* **1969,** *30* (7), 1823-1825.

30. Petschnig, L. L.; Fuhrmann, G.; Schildhammer, D.; Tribus, M.; Schottenberger, H.; Huppertz, H., Solution combustion synthesis of CeFeO3 under ambient atmosphere. *Ceram. Int.* **2016,** *42* (3), 4262-4267.

31. Shen, K.; Fan, M.; Kwon, O.; Viescas, A. J.; Papaefthymiou, G. C.; Gorte, R. J.; Vohs, J. M., Reversible perovskite-fluorite phase transition in alumina-supported CeFeOx films. *J. Mater. Chem. A* **2023,** *11* (8), 4183-4193.

32. Singh, V.; Muroyama, H.; Matsui, T.; Hashigami, S.; Inagaki, T.; Eguchi, K., Feasibility of alternative electrode materials for high temperature CO2 reduction on solid oxide electrolysis cell. *J. Power Sources* **2015,** *293*, 642-648.

33. Scandolo, S.; Giannozzi, P.; Cavazzoni, C.; Gironcoli, S. d.; Pasquarello, A.; Baroni, S., First-principles codes for computational crystallography in the Quantum-ESPRESSO package. **2005,** *220* (5-6), 574-579.

34. Miyashita, T.; Kobayashi, Y.; Fukamachi, T.; Masuda, H.; Sato, M., Spin-state change of Co atoms of $La_4Co_3O_{10+\delta}$. *Physica B.* **2003,** *329*, 740-742.

35. Huang, X.; Ni, C.; Zhao, G.; Irvine, J. T. S., Oxygen Storage Capacity and Thermal Stability of $CuMnO_2$-$CeO_2$ Composite System. *J. Mater. Chem. A* **2015,** *3*, 12958-12964.

36. Jiang, Y.; Chen, F.; Xia, C., A review on cathode processes and materials for electro-reduction of carbon dioxide in solid oxide electrolysis cells. *J. Power Sources* **2021,** *493*, 229713.

37. Nie, X.; Wang, H.; Li, W.; Chen, Y.; Guo, X.; Song, C., DFT insight into the support effect on the adsorption and activation of key species over Co catalysts for CO2 methanation. *J. CO2 Util.* **2018,** *24*, 99-111.

38. Albrecht, P. M.; Jiang, D.-e.; Mullins, D. R., CO2 Adsorption As a Flat-Lying, Tridentate Carbonate on CeO2(100). *J. Phys. Chem. C* **2014,** *118* (17), 9042-9050.

39. Skorodumova, N. V.; Baudin, M.; Hermansson, K., Surface properties of ${\mathrm{CeO}}_{2}$ from first principles. *Physical Review B* **2004,** *69* (7), 075401.

40. Kilic, M. E.; Lee, J.-H.; Lee, K.-R., Oxygen ion transport in doped ceria: effect of vacancy trapping. *J. Mater. Chem. A* **2021,** *9* (24), 13883-13889.

41. Hahn, K. R.; Iannuzzi, M.; Seitsonen, A. P.; Hutter, J., Coverage Effect of the CO2 Adsorption Mechanisms on CeO2(111) by First Principles Analysis. *J. Phys. Chem. C* **2013,** *117* (4), 1701-1711.

42. Feng, W.; Song, Y.; Zhang, X.; Lv, H.; Liu, Q.; Wang, G.; Bao, X., Platinum-Decorated Ceria Enhances CO2 Electroreduction in Solid Oxide Electrolysis Cells. *ChemSusChem* **2020,** *13* (23), 6290-6295.

43. Irvine, J. T. S.; Xie, K., Enhanced CO2 Electrolysis at Redox Engineered Interfaces. *ECS Trans.* **2019,** *91* (1), 2565-2570.

44. Liu, C. Y.; Li, S. T.; Gao, J. Q.; Bian, L. Z.; Hou, Y. T.; Wang, L. J.; Peng, J.; Bao, J. X.; Song, X. W.; An, S. L., Enhancing $CO_2$ Catalytic Adsorption on an Fe Nanoparticle-Decorated $LaSrFeO_{4+\delta}$ Cathode for CO2 Electrolysis. *ACS Appl. Energ. Mater.* **2021,** *13* (7), 8229-8238.

45. Cao, Z. Q.;   Wei, B.;   Miao, J. P.;   Wang, Z. H.;   Lu, Z.;   Li, W. Y.;   Zhang, Y. H.;   Huang, X. Q.;   Zhu, X. B.;   Feng, Q.; Sui, Y., Efficient electrolysis of CO2 in symmetrical solid oxide electrolysis cell with highly active La0.3Sr0.7Fe0.7Ti0.3O3 electrode material. *Electrochem. Commun.* **2016,** *69*, 80-83.

46. Wang, S.;   Jiang, H. G.;   Gu, Y. H.;   Yin, B.;   Chen, S. N.;   Shen, M. Y.;   Zheng, Y. F.;   Ge, L.;   Chen, H.; Guo, L. C., Mo-doped $La_{0.6}Sr_{0.4}FeO_{3-\delta}$ as an efficient fuel electrode for direct electrolysis of $CO_2$ in solid oxide electrolysis cells. *Electrochim. Acta* **2020,** *337*, 135794.

47. Tian, Y. F.;   Zheng, H. Y.;   Zhang, L. L.;   Chi, B.;   Pu, J.; Li, J., Direct Electrolysis of $CO_2$ in Symmetrical Solid Oxide Electrolysis Cell Based on $La_{0.6}Sr_{0.4}Fe_{0.8}Ni_{0.2}O_{3-delta}$ Electrode. *J. Electrochem. Soc.* **2018,** *165* (2), F17-F23.

48. Lv, H.;   Liu, T.;   Zhang, X.;   Song, Y.;   Matsumoto, H.;   Ta, N.;   Zeng, C.;   Wang, G.; Bao, X., Atomic-Scale insight into exsolution of CoFe alloy nanoparticles in $La_{0.4}Sr_{0.6}Co_{0.2}Fe_{0.7}Mo_{0.1}O_{3-\delta}$ with efficient $CO_2$ electrolysis. *Angew. Chem. Int. Edit.* **2020,** *59* (37), 15968-15973.

49. Zhu, C. L.;   Hou, S. S.;   Hou, L. X.; Xie, K., Perovskite $SrFeO_{3-\delta}$ decorated with Ni nanoparticles for high temperature carbon dioxide electrolysis. *Int. J. Hydrogen Energ.* **2018,** *43* (36), 17040-17047.

50. Zhang, J.;   Xie, K.;   Zhang, Y.;   Yang, L. M.;   Wu, G. J.;   Qin, Q. Q.;   Li, Y. X.; Wu, Y. C., Composite titanate cathode decorated with heterogeneous electrocatalytic sites towards efficient carbon dioxide electrolysis. *RSC Adv.* **2014,** *4* (43), 22697-22709.

51. Lv, H. F.;   Lin, L.;   Zhang, X. M.;   Song, Y. F.;   Matsumoto, H.;   Zeng, C. B.;   Ta, N.;   Liu, W.;   Gao, D. F.;   Wang, G. X.; Bao, X. H., In Situ Investigation of Reversible Exsolution/Dissolution of CoFe Alloy Nanoparticles in a Co-Doped $Sr_2Fe_{1.5}Mo_{0.5}O_{6-delta}$ Cathode for $CO_2$ Electrolysis. *Adv. Mater.* **2020,** *32* (6).

52. Li, Y. H.;   Chen, X. R.;   Yang, Y.;   Jiang, Y. N.; Xia, C. R., Mixed-Conductor $Sr_2Fe_{1.5}Mo_{0.5}O_{6-\delta}$ as Robust Fuel Electrode for Pure $CO_2$ Reduction in Solid Oxide Electrolysis Cell. *ACS Sustain. Chem. Eng.* **2017,** *5* (12), 11403-11412.

53. Ma, G.;   Xu, Y.; Xie, K. Enhanced Electrolysis of $CO_2$ with Metal&ndash;Oxide Interfaces in Perovskite Cathode in Solid Oxide Electrolysis Cell *Catalysts* [Online], 2022, p. 1607.

54. Zhou, Y.;   Zhou, Z.;   Song, Y.;   Zhang, X.;   Guan, F.;   Lv, H.;   Liu, Q.;   Miao, S.;   Wang, G.; Bao, X., Enhancing $CO_2$ electrolysis performance with vanadium-doped perovskite cathode in solid oxide electrolysis cell. *Nano Energy* **2018,** *50*, 43-51.

55. Yang, X.;   Sun, K.;   Ma, M.;   Xu, C.;   Ren, R.;   Qiao, J.;   Wang, Z.;   Zhen, S.;   Hou, R.; Sun, W., Achieving strong chemical adsorption ability for efficient carbon dioxide electrolysis. *Appl. Catal. B* **2020,** *272*, 118968.

56. Li, Y.;   Chen, X.;   Yang, Y.;   Jiang, Y.; Xia, C., Mixed-Conductor $Sr_2Fe_{1.5}Mo_{0.5}O_{6-\delta}$ as Robust Fuel Electrode for Pure $CO_2$ Reduction in Solid Oxide Electrolysis Cell. *ACS Sustain. Chem. Eng.* **2017,** *5* (12), 11403-11412.

57. Yudanov, I. V.;   Genest, A.;   Schauermann, S.;   Freund, H.-J.; Rösch, N., Size Dependence of the Adsorption Energy of CO on Metal Nanoparticles: A DFT Search for the Minimum Value. *Nano Lett.* **2012,** *12* (4), 2134-2139.

58. Taylor, M. G.;   Austin, N.;   Gounaris, C. E.; Mpourmpakis, G., Catalyst Design Based on Morphology- and Environment-Dependent Adsorption on Metal Nanoparticles. *ACS Catal.* **2015,** *5* (11), 6296-6301.

59. Wang, J.;   Kalaev, D.;   Yang, J.;   Waluyo, I.;   Hunt, A.;   Sadowski, J. T.;   Tuller, H. L.; Yildiz, B., Fast Surface Oxygen Release Kinetics Accelerate Nanoparticle Exsolution in Perovskite Oxides. *J. Am. Chem. Soc.* **2023,** *145* (3), 1714-1727.

60. Gorte, R. J.; Vohs, J. M., Catalysis in solid oxide fuel cells. *Annu. Rev. Chem. Biomol.* **2011,** *2* (1), 9-30.

61. Su, Y.-Q.;   Xia, G.-J.;   Qin, Y.;   Ding, S.; Wang, Y.-G., Lattice oxygen self-spillover on reducible oxide

supported metal cluster: the water–gas shift reaction on Cu/CeO2 catalyst. *Chemical Science* **2021,** *12* (23), 8260-8267.